

# Simulation of Large-Area Silicon Solar Cells<sup>1</sup>

Gernot Heiser<sup>2</sup>      Pietro P. Altermatt<sup>3</sup>  
The University of NSW, Sydney 2052, Australia.

UNSW-CSE-TR-9505 — 12 December 1995

<sup>1</sup>This work was supported by a grant from the Australian Research Council (ARC). The Centre for Photovoltaic Devices and Systems is supported by Pacific Power and the ARC.

<sup>2</sup>School of Computer Science and Engineering, tel: +61 2 385 5156, fax: +61 2 385 5995, e-mail: G.Heiser@unsw.edu.au

<sup>3</sup>Centre for Photovoltaic Devices and Systems, tel: +61 2 385 5471, fax: +61 2 662 4240, e-mail: pietro@vast.unsw.edu.au

## **Abstract**

Two- and three-dimensional numerical modelling has recently become an important tool for the characterisation and optimisation of high-efficiency silicon solar cells. In the past, however, such modelling could only be applied to small sections of the cells. While such limited simulation domains are sufficient for the analysis of bulk and surface properties, the analysis and optimisation of effects like the losses resulting from the resistance of the metal contact grid require a model of the full cell and need to include edge effects. In this paper, we present an approach which combines multi-dimensional device simulation with circuit simulation to produce an accurate model of a full-sized high-efficiency solar cell. We demonstrate the power of this approach by presenting the results of an investigation of the series resistance of “passivated emitter, rear locally diffused” (PERL) silicon solar cells. The insights gained in that study triggered a small design change in the contact geometry, which managed to reduce resistive losses by more than half and contributed to a new efficiency world record.

# 1 Introduction

Since early 1993 multi-dimensional numerical simulations have been used extensively at the University of New South Wales (UNSW) for the study of the present generation of high-efficiency silicon solar cells manufactured there. The specific aims of the project were the characterization and quantification of all losses limiting the conversion efficiencies of these cells, and the optimization for highest cell efficiency. The effort contributed significantly to the recent improvement of the efficiency world record for silicon solar cells at unconcentrated (“1-sun”) illumination to 24 % [1, 2].

These simulations face significant obstacles: the required simulation domains are very large, while some features that need to be resolved are only nanometres big [3]. A full analysis of losses requires 3D simulations and the incorporation of edge effects.

Because of these problems, multi-dimensional device simulations have, until recently, not been very prominent in high-efficiency silicon solar cell design and analysis. One exception to this was the work of Gray et al. [4], who showed the existence of 2D-effects in silicon concentrator cells, where such effects are much stronger than in one-sun cells. Such concentrator cells are several orders of magnitude smaller than 1-sun cells, which makes numerical treatment much easier. Recently, 2D [3, 5] and 3D [6–10] simulations of high-efficiency one-sun silicon solar cells have been reported. These all focused on particular effects that only required a limited simulation domain corresponding to a small fraction of a cell. Most of these approaches also involved simplifications and assumptions which limit the applicability of their method.

This paper reports on an approach to the accurate determination and analysis of the series resistance,  $R_s$ , which is an important factor limiting the performance of high-efficiency silicon solar cells. To determine  $R_s$  we had to model a full,  $2 \times 2 \text{ cm}^2$ , silicon solar cell to a high level of accuracy. This unique achievement was made possible by an innovative approach, which combines circuit simulation with multidimensional device simulation in a model of a single device.

The remainder of the paper is organized as follows: Section 2 gives a short introduction in the operation of solar cells in general, and high-efficiency silicon solar cells in particular. In Section 3 we present the methods used to model the behaviour of our high-efficiency silicon solar cells. Section 4 contains the results of our simulations and compares them to experimental data. In Section 5 we present our conclusions.

## 2 High-Efficiency Silicon Solar Cells

### 2.1 Solar cell operation

Solar cells generate electricity from sunlight. The absorption of photons of sufficient energy creates mobile electron-hole pairs in the semiconductor material. If

these carriers are captured by separate electrodes, their energy can be used to deliver power to an external load. In order to be collected, the electron-hole pairs must be separated by an electric field before recombining again. In all present high-efficiency devices a p-n junction is used to create such a separating field.

Thus a solar cell can be thought to consist of a diode connected in parallel to a current source, which supplies the light-generated current,  $J$ . The resulting ideal current-voltage (J-V) characteristic is therefore that of an ideal diode shifted by  $J$ :

$$J(V) = J_0 \left[ \exp\left(\frac{qV}{nk_B T}\right) - 1 \right] - J_l, \quad (1)$$

where  $V$  is the external voltage,  $q$  the elementary charge,  $k_B$  the Boltzmann constant,  $T$  the temperature,  $J_0$  the saturation current and  $n$  the ideality factor. Figure 1 shows typical J-V and power-voltage (P-V) curves of a cell. Since  $P = JV$ , the cell delivers its maximum power output at a unique *maximum power point* (MPP), i.e. at  $V_{mpp}$  and  $J_{mpp}$ .

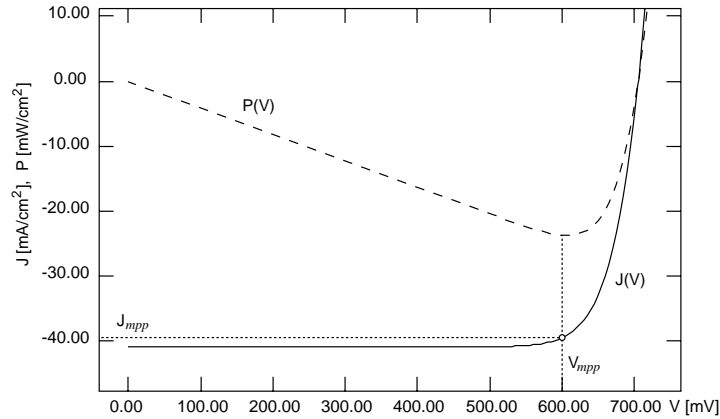


Figure 1: Typical J-V and P-V curves of a solar cell.

The *efficiency*,  $\eta$ , of a solar cell is given as

$$\eta = \frac{P_{mpp}}{P_l} = \frac{FF J_{sc} V_{oc}}{P_l}, \quad (2)$$

where  $P_{mpp} = J_{mpp} V_{mpp}$  and  $P_l$  is the power of the incoming light flux. It is useful to express  $P_{mpp}$  in terms of the cell's *short-circuit current*,  $J_{sc} = J(V=0)$ , the *open-circuit voltage*,  $V_{oc}$ , and the *fill factor*,  $FF = J_{mpp} V_{mpp} / J_{sc} V_{oc}$ .

$J_{sc}$  is sensitive to the amount of sunlight the cell is able to convert into electric current, and is thus dependent, e.g., on the cell's absorption and reflection properties.  $V_{oc}$  is strongly degraded by electron-hole pairs lost to recombination. The fill factor is only slightly influenced by recombination, but is very sensitive to *resistive losses*, which reduce  $V_{mpp}$ . For more details on solar cell operation, see [11, 12].

Note that, in general, logarithmic plots of diode characteristics are more informative than linear ones, as the former are straight lines for ideal diodes. The J-V curve of a solar cell under illumination can be similarly represented if it is first shifted into the first quadrant by adding  $J_{sc}$  [13] (which, for all practical purposes, is the same as  $J_l$ ).<sup>1</sup> All illuminated J-V curves shown in the remainder of this paper are shifted by  $J_{sc}$ .

## 2.2 Characteristics of high-efficiency silicon solar cells

A typical representative of high-efficiency silicon solar cells is the *passivated emitter, rear locally diffused* (PERL) silicon solar cell, developed at the Centre for Photovoltaic Device and Systems at the University of New South Wales (UNSW). This design has demonstrated an independently-confirmed efficiency of 24.0% [1], the highest ever recorded for a silicon solar cell under unconcentrated terrestrial illumination (so-called *air mass 1.5 global*, AM1.5G, spectrum, normalized to  $P_i = 100 \text{ mW/cm}^2$ ). PERL cells presently reach  $J_{sc}$  values of around 40–41  $\text{mA/cm}^2$ , a  $V_{oc}$  of 700–710 mV, and a  $FF$  of around 81–83%.

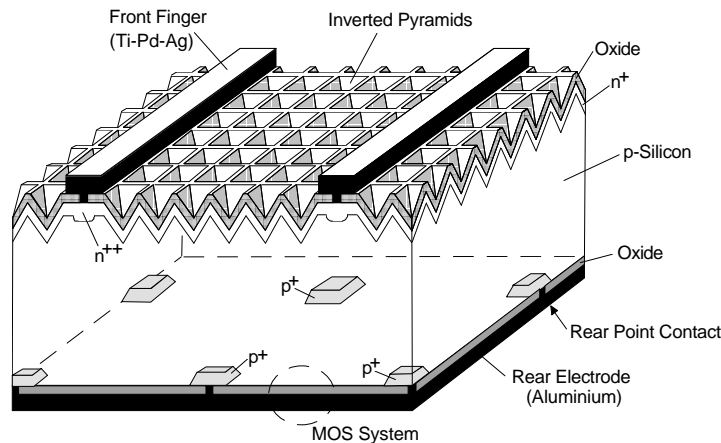


Figure 2: Schematic drawing of a section of the PERL high-efficiency silicon solar cell.

The cell is manufactured from a monocrystalline p-type wafer of 250–400  $\mu\text{m}$  thickness, typically doped at  $1.4 \times 10^{16} \text{ cm}^{-3}$ , resulting in a resistivity of 1  $\Omega\text{cm}$ . In order to create an  $n^+p$  diode, phosphorous is diffused into the top surface, forming the so-called *emitter* with a thickness of approximately 1  $\mu\text{m}$  and a peak doping concentration of  $5 \times 10^{18} \text{ cm}^{-3}$ . The remaining substrate region forms the so-called *base*.

<sup>1</sup>In an ideal diode, such a shifted illuminated J-V curve would be identical to the unshifted dark one.

Silicon exhibits a low absorption rate for red and near infrared light, with mean path lengths up to 10 cm, while blue light gets mostly absorbed within the first 10 nm. To enhance the absorption of long wavelength light, the front surface of the cell is textured with “inverted” pyramids (obtained by anisotropic etching). This results in a partial “capture” of the incoming light due to enhanced internal reflection, and also reduces external reflection at the front surface.

External reflection is also minimised by using thin and widely-spaced front contact fingers. The finger spacing is limited by the finite conductivity of the thin emitter layer, which needs to conduct the bulk of the light-generated electrons to the contact. Thin metal fingers also increase resistive losses. Typical values for PERL cells are 20  $\mu\text{m}$  finger width and 800  $\mu\text{m}$  finger spacing.

Further cell features evident in Figure 2 are aimed at reducing recombination losses. These are:

- High-quality substrate material, so-called *float zone* silicon, featuring minority carrier lifetimes of the order of 2 ms,
- High-quality thermal oxide to passivate the front and rear surfaces. Typical surface recombination velocities are 2000 cm/s at the highly doped front and 50 cm/s at the rear surface,
- Minimal metal-semiconductor interface areas, as these are effective recombination centres. The front metal interface is 3  $\mu\text{m}$  wide (although the fingers are 20  $\mu\text{m}$  wide). This corresponds to a metallisation fraction of < 0.4 %. The rear features point contacts of  $10 \times 10 \mu\text{m}^2$  (metallization fraction 0.016 %),
- Highly doped diffusions under the contacts,  $10^{20} \text{ cm}^{-3}$  at the emitter and  $5 \times 10^{18} \text{ cm}^{-3}$  at the base contacts.

### 3 Simulation of High-Efficiency Silicon Solar Cells

#### 3.1 Standard model

If edge effects and the resistivity of the front metal fingers can be ignored, symmetry reduces the simulation domain to an *irreducible* section, the horizontal dimensions of which are defined by half the (front and rear) contact spacings, while vertically, the whole device needs to be simulated (see Figure 3). For a typical PERL cell these dimensions are  $800 \times 370 \times 167 \mu\text{m}^3$ . We refer to this simulation volume as a *standard domain*.

The 3D front surface texture presents a number of problems for the simulation: resolution of the geometrical features results in very large simulation grids, and the proper determination of photogeneration rates requires sophisticated ray-tracing. However, we found that the following simplified approach produces excellent results. We use a flat front surface for the device simulations. However, we assume

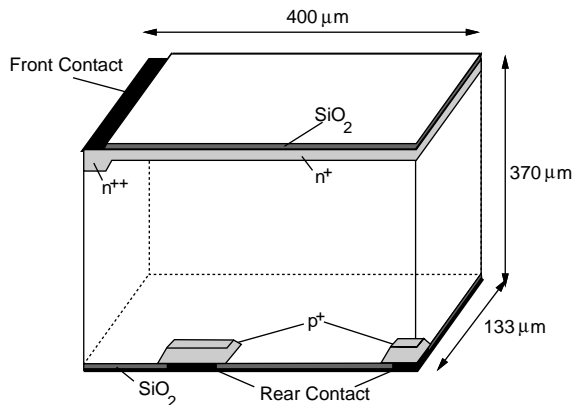


Figure 3: Simulation domain for 3D simulation of PERC cells.

light to be coupled into the device at angles equal to those produced by the inverted pyramid texture, thereby reproducing the path-length enhancement resulting from the surface texture. Internal reflection at the front and rear surfaces are treated by wavelength-independent reflectivities, and light remaining after two full passes through the cell is assumed to be absorbed homogeneously throughout the cell, as in [14]. We then adjust the intensity of the incoming light to fit the measured  $J_c$  value. This approach will be discussed in more detail in a forthcoming publication [15].

While, with these simplifications, the emitter region of a PERC cell is 2D, the rear contact pattern, and hence the current distribution in the base, is truly 3D. These 3D effects are rather mild, and not relevant in most cases: an optimisation study of the rear contact spacing [16], which was based on 2D simulation, produced similar results of the optimal spacing as subsequent 3D studies [9, 17]. However, for the determination and characterisation of  $R_s$ , the resistive effect of the crowding of the hole current around the rear contacts needs to be accurately modelled. Hence 3D simulations are necessary in this case.

Figure 4 shows a typical simulation mesh of a standard domain. The Figure cannot show the full extent of the grid refinement at the front surface, where a vertical mesh point spacing as low as 1 nm is required to resolve the exponential decay of photo-generation. At the rear surface a 10 nm spacing of mesh lines is required to resolve an inversion layer resulting from oxide charges and the Si-Al work function difference [18]. The mesh shown consists of approximately 60,000 vertices. 3D domains much larger than the standard domain are obviously unfeasible.

Contributions to  $R_s$  arising from the front metal fingers cannot be assessed at all by simulations of the standard domain, so an extended model of the solar cell is required to account for these effects.

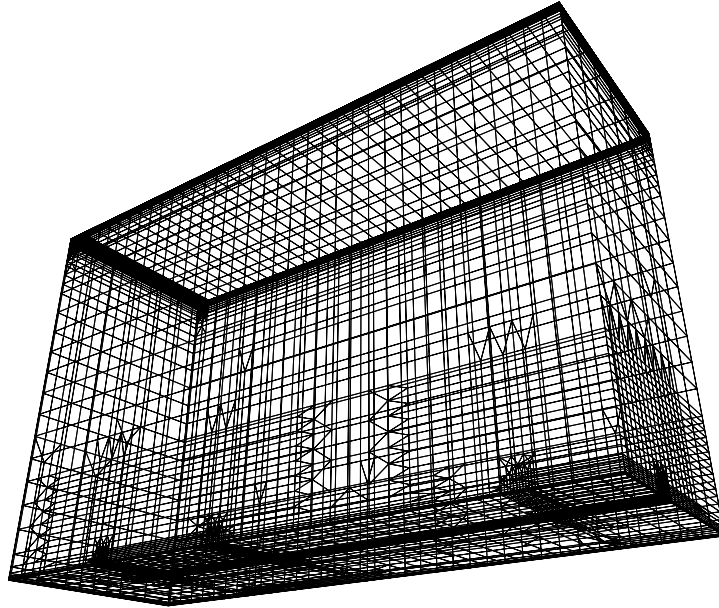


Figure 4: 3D simulation mesh of a standard domain. The refinements around the rear contacts can be seen at the bottom of the picture. A front contact is located at the top left indicated by the highly refined (black) region.

### 3.2 Contact finger resistivity

It is not possible to measure the ohmic resistance of the front contact fingers accurately. In the past, therefore, the simulated J-V curves were compared to experiments in a resistance-free representation. The measured J-V characteristics were corrected by the measured (total) resistance, while the simulated characteristics were corrected by the simulated (internal) resistance. Although this procedure has been used successfully in the analysis of the non-ideal J-V characteristics of PERL cells [16], it is not appropriate for  $R_s$  optimisation studies. The main reason for this is that the so-called *non-generation loss*, which contributes to  $R_s$ , cannot be determined without knowledge of the actual voltage profile along the front metal grid of a cell.

The non-generation loss results from the voltage drop along the metal fingers, which implies that it is impossible for the *whole* cell to operate under local MPP condition with any fixed external bias. If the cell is operated at the global MPP bias, where the total power output is maximized, some parts of the cell will operate at higher, and others at lower than local MPP bias, and therefore produce less a than optimal power output. Owing to this effect, the losses due to the finite conductivity of the metal grid are larger than those resulting from Joule heating.

### 3.3 Extended model

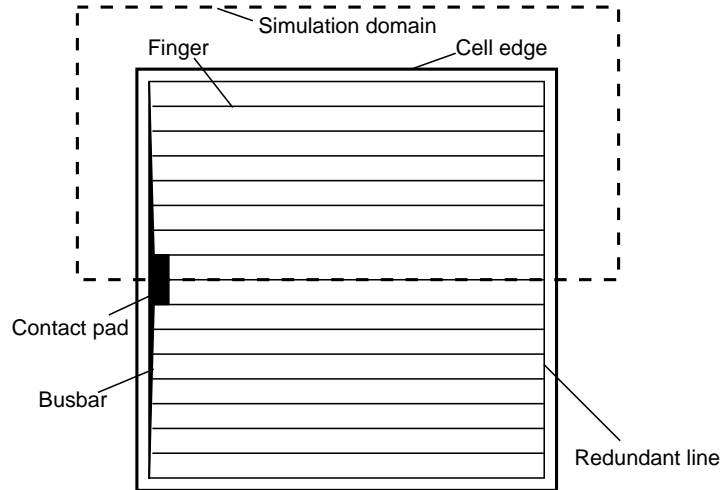


Figure 5: Front contact grid pattern of a PERL cell.

Figure 5 shows the geometry of the contact grid of a PERL cell. For symmetry reasons only half the grid must be modelled. A 3D device simulation of such a domain, measuring  $10 \times 20 \times 0.37 \text{ mm}^3$ , is impossible on present computers—the memory and time requirements would be enormous. Instead we make use of the fact that the interior of the cell, i.e. everything inside the region defined by the metal grid, can be thought of as being “tiled” with standard domains, as indicated in Figure 6. The whole interior of the extended simulation domain of a typical PERL cell consists of about 3000 identical standard domains. At corners where the contact fingers meet the collecting *bus bar* or the *redundant line* (cf. Figure 5), modified standard domains need to be used.

Under the assumption that there is *negligible current flow* within the semiconductor *between any two of these standard domains*, it is possible to treat them in isolation. This condition is satisfied quite well, as the voltage drop along the front finger within each domain is negligible for a well-designed cell with a reasonably small finger resistivity. Similarly, the voltage difference between two neighbouring fingers is sufficiently small (compare Section 4).

We can thus consider a PERL cell to be a circuit consisting of (mostly) identical devices, corresponding to standard sections of the cell, connected by resistors representing the metal grid. The behaviour of the individual standard sections is represented by their respective J-V curves, which can be obtained from 3D device simulations. The J-V curve of the whole device can then be obtained from a circuit simulation [19].

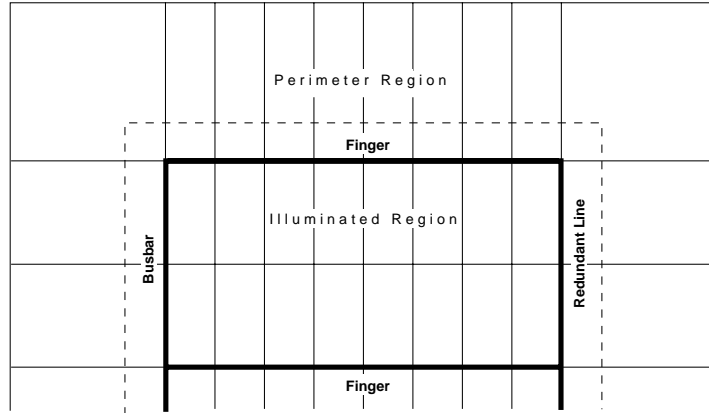


Figure 6: Coverage of PERL cell with 3D simulation domains. The dashed line defines the illuminated area.

### 3.4 Edge effects

The PERL cells remain embedded in the wafer when their efficiency is measured. This is done to avoid performance degradation resulting from the damage inflicted by cutting a wafer with lasers or mechanical saws. However, even such an “open” perimeter degrades cell performance. Carriers diffuse across the boundary of the illuminated cell area where they are eventually lost by recombination. Estimates based on simple analytical models predict a degradation of  $V_{oc}$  of about 6 mV in  $2 \times 2 \text{ cm}^2$  cells [13].

The active perimeter region is quite large. Minority carrier diffusion lengths in PERL cells are around 2 mm, and we observe that a cell’s J-V curve is influenced by another cell in the same wafer 5 mm away! While this is an extreme case with no real practical significance (other than showing that care is required when performing measurements), a proper treatment of perimeter effects requires the inclusion of a sizable dark region in the cell model. We found that including a 3 mm-wide strip of perimeter region surrounding the illuminated cell area was required to obtain converged results for the overall cell characteristics.

A domain of this size is, again, far too big for a 3D simulation. However, the perimeter region is essentially 2D. Even though the rear contacts in this area are still point-like, and thus 3D, the current densities are very small, so that current crowding is insignificant and a 2D treatment is appropriate. This poses the question of how 2D simulations of perimeter effects can be combined with 3D simulations of the illuminated cell areas in a consistent fashion.

We decided to treat the shaded region as a perturbation of the illuminated region, assuming that the perimeter effect can be superimposed onto the behaviour of a standard domain. We thus perform a 2D simulation of a perimeter domain as shown in Figure 7, yielding  $J_{2D,p}(V)$ , and a 2D ( $J_{2D,s}(V)$ ) as well as a 3D

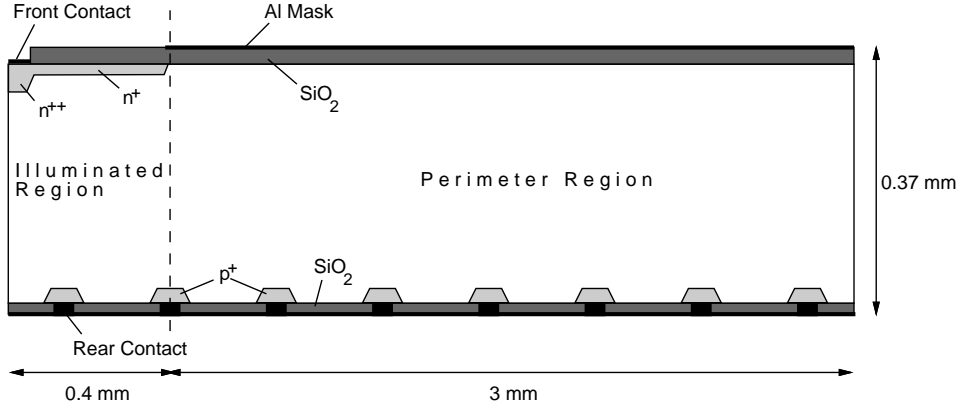


Figure 7: Simulation domain for the modelling of perimeter effects. The part to the left of the dashed line is identical to a (2D) standard domain.

( $J_{3D,s}(V)$ ) simulation of a standard domain. The J-V curve of a standard domain at the perimeter of the cell can then be approximated as

$$J_{3D,p}(V) \approx J_{3D,s}(V) + (J_{2D,p}(V) - J_{2D,s}(V)), \quad (3)$$

provided that all currents are in units of  $\text{mA}/\text{cm}^2$  of *illuminated cell area*.

We checked the validity of our assumptions by performing a 2D simulation of a perimeter domain extended by one standard domain into the interior of the cell. If our assumptions hold, the J-V curve resulting from such a simulation should be the same as the sum of the J-V curves of a 2D standard domain and a 2D perimeter domain. It can be seen from Figure 8 that the current patterns of the two cases are quite similar. The main difference is that the region of low current density below the front contact finger is less pronounced below the outermost finger in the extended perimeter domain simulation. This difference results from a current flow across this area into the perimeter region; in the standard domain simulation, the boundary conditions prevent such a current flow out of the simulation domain. The magnitude of this current, according to the extended perimeter simulation, is  $5.2 \mu\text{A}$  per cm of cell perimeter near MPP. This corresponds to 0.15% of the total current of the outermost finger and is therefore negligible. Figure 9 confirms that the simulation of an extended perimeter domain gives a current that is very close to that of a standard domain combined with a standard perimeter domain. The agreement is particularly good in the important region between  $V_{mpp}$  and  $V_{oc}$  (600–700 mV).

There remains the question of how to deal with corners. There are two types (cf. Figure 6): *Internal corners*, where a finger meets the busbar or the redundant line, and *external corners*, the outer corners where the outermost finger meets the end of the bus bar or the redundant line. There are four internal corners per interior finger, and a total of two external ones.

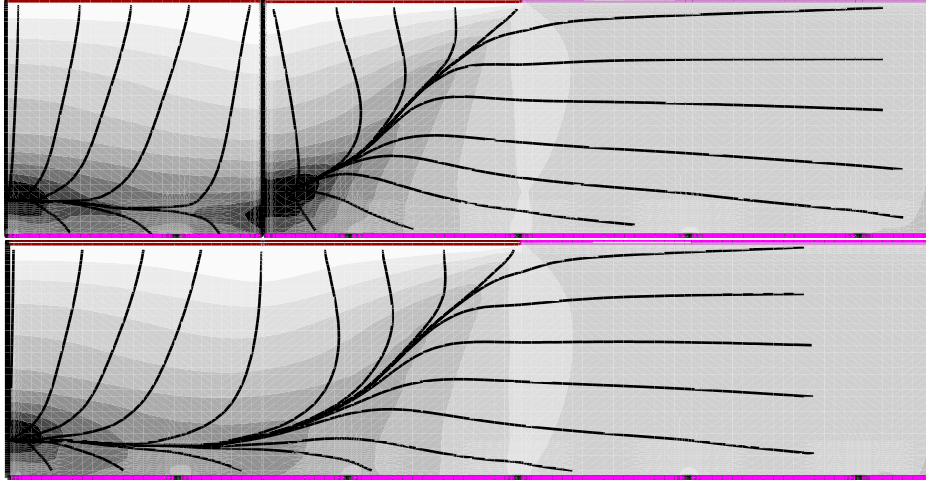


Figure 8: Electron current density near MPP according to an extended (by one standard domain) 2D perimeter simulation (bottom), compared to the current density of a standard domain simulation (top left) and a normal perimeter simulation (top right).

The internal corners can be dealt with by using a modified standard domain where the front contact runs along two sides instead of just one. However, we found that it was possible to obtain the same results from a standard domain. When the light intensity was reduced to account for the increased shading resulting from the larger contact area, the resulting J-V curve became indistinguishable from that of a proper corner domain.

An accurate treatment of external corners of the device would require a more sophisticated 3D model. However, the contributions of these two regions to the behavior of the full cell is very small, and we instead use a simplified approach, applying the 2D perimeter correction twice to a standard domain, yielding the J-V curve of the 3D corner section as

$$J_{3D,c}(V) \approx J_{3D,s}(V) + 2(J_{2D,p}(V) - J_{2D,s}(V)) \quad (4)$$

This simplification is justified, as we found that completely ignoring the two corner sections only had a minimal influence on the total J-V curve.

### 3.5 Simplification of circuit simulations

It has been mentioned earlier that a full scale PERL cell model consists of a circuit of 3000 devices representing sections of a PERL cell. Together with the resistors representing the metal grid, this would require a simulation of a circuit consisting of some 6000 devices. However, far fewer devices need to be used in the actual circuit simulations.

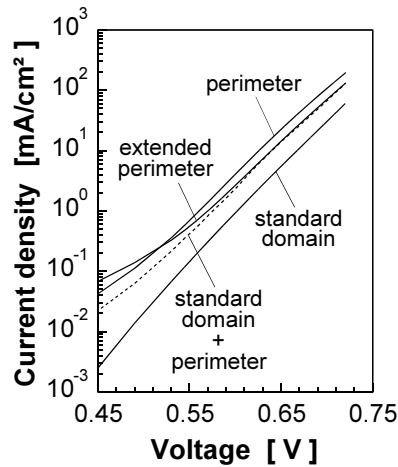


Figure 9: Comparison of 1-sun current density resulting from an extended perimeter domain with that of a perimeter domain combined with a standard domain.

Firstly we observe that at each node of the circuit, several devices are connected in parallel. For example, along an internal contact finger there is one standard domain at each side of the finger, corresponding to two standard devices in our circuit model. As these are identical, it is sufficient to use just one and double its current. Similarly, along the outermost finger, at each circuit node a standard domain and a perimeter domain are connected in parallel. Their currents can again be added, reducing the number of independent devices in the circuit simulation by approximately a factor of two to 1534, plus a similar number of resistors (see Figure 10).

Secondly, we observe that the resulting circuit is really a discretisation of a PERL cell (cf. Figure 6), and we can adjust the discretisation error by varying the coarseness of the discretisation. We found that when using 12 nodes to represent the interior parts of each metal finger, we obtained a current that was converged to at least four digits. This reduces the size of the circuit simulation to 156 PERL cell devices and a similar number of resistors.

The busbar of a PERL cell is tapered to adjust its resistivity to the current it needs to conduct (cf. Figure 5). This represents a further complication with the simulation, as we ought to use “standard” devices with different sizes of the shaded regions. However, as the total area of the busbar is only 0.56% of the total cell area, we instead just increase the dark area of the cell by the difference between the area of the busbar and the area of one of the other fingers. This is consistent with our treatment of internal corners. The graded resistivity of the busbar is properly taken into account by varying the size of the resistors representing the busbar. The redundant line is of the same width as the normal fingers, and therefore requires no special treatment.

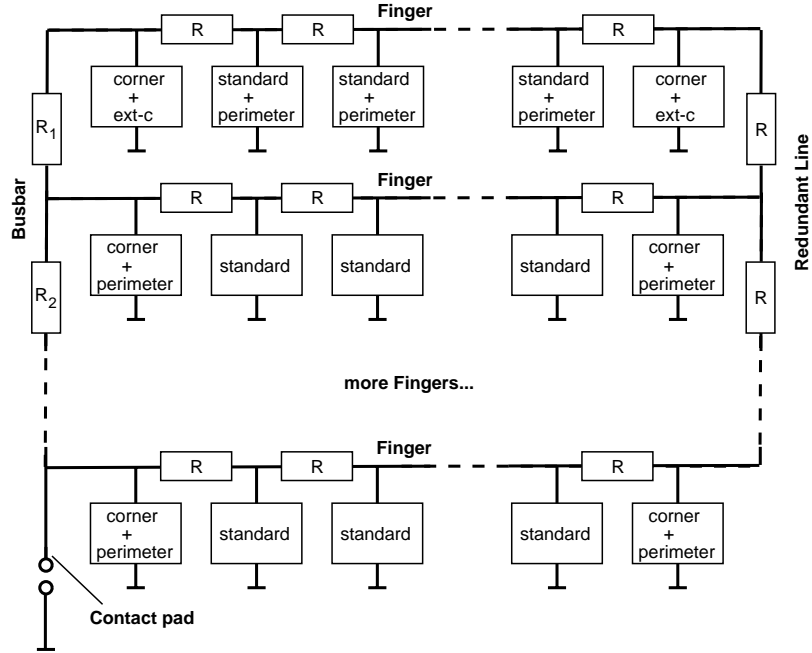


Figure 10: Circuit used to simulate a full PERL cell. The boxes symbolise the results of 3D device simulations which are represented by their J-V curve. “Corner” devices are “standard” devices scaled to account for the reduced illuminated area, while “ext-c” indicates an external corner device modelled according to Eq. 4.

### 3.6 Optimisation of resistive losses

In order to compute a J-V curve of a full PERL cell at a particular illumination level, we need to run one of each of the previously discussed simulation types. The determination of  $R_s$  requires two J-V curves,  $J^{(a)}(V)$  and  $J^{(b)}(V)$ , determined at slightly different illumination levels. One of the curves is shifted, by  $\Delta J_c = J^{(a)}(0) - J^{(b)}(0)$ , so that the short-circuit currents agree. The series resistance is then given as [20]:

$$R_s(V) = \frac{\Delta V}{\Delta J_{sc}}, \quad (5)$$

where  $\Delta V$  is the distance between the curves in  $V$  direction at voltage  $V$ .

All device and circuit simulations were performed using the mixed-mode device and circuit simulator DESSIS [21]. Device simulation in DESSIS is based on the box-method, and the package includes a powerful tool for generating highly adaptive grids—an essential requirement for our work. We did not use the possibility provided by DESSIS to couple device and circuit modelling in a single simulation run, as this would have been too expensive in our case. Instead we performed the device simulations first, extracted the J-V curves, and then fed these into a separate circuit simulation.

Figure 11: Voltage profile of PERL cell w413-9 at maximum power point conditions, simulation (left) vs. measurement (right).

Figure 11 compares the simulated voltage profile of a PERL cell at the maximum power point with the measured one. For the device simulations we used mostly measured parameters [13, 16]. The bulk lifetimes cannot be measured experimentally in a manufactured cell. We therefore used them as a fitting parameter to match the experimentally observed  $V_{oc}$  value. The resulting curve fit is shown in Figure 12. For details see [18].

Furthermore, the finger and busbar resistivities can only be measured with significant inaccuracy. We therefore used these as another fitting parameter, this time to match the voltage profile of Figure 11. It can be clearly seen that excellent agreement was achieved.

Applying Eq. 5 to the simulated J-V curve yields the cell's total series resistance. The resulting  $R_s$  values match the experimentally determined ones to an unprecedented level of accuracy (Figure 13).

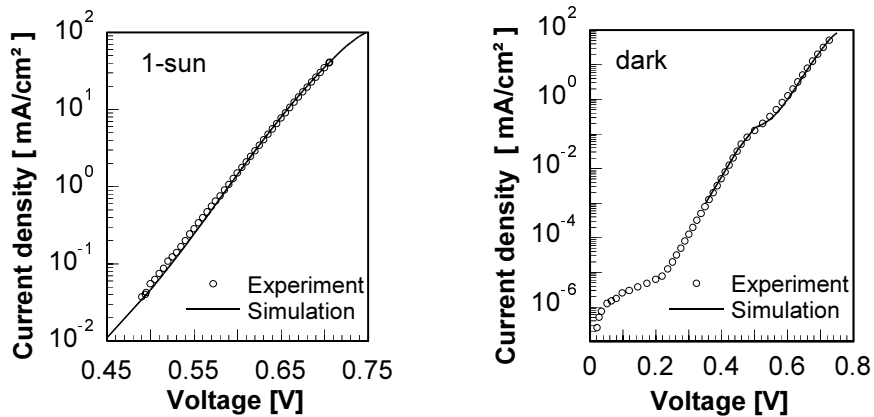


Figure 12: Comparison of measured and simulated I-V curves of cell w413-9 under 1-sun illumination (left) and in the dark (right).

From our simulations we obtained a fairly accurate value of  $R_{\text{g}} = 0.49 \Omega \text{ cm}^2$  at 1-sun MPP, which corresponds to a loss of  $0.715 \text{ mW/cm}^2$ . Of this,  $0.482 \text{ mW/cm}^2$  (67 %) turned out to be due to the contact grid resistivity. Joule heating accounted for 54 % of the latter loss, non-generation for 46 %. The contribution of the emitter to the total resistive loss is 23 %, while that of the base is 10 %.

The quantification and improved understanding of the resistive losses enabled us to optimise separately the contributions to  $R_{\text{g}}$  of the various parts of the device. For example, Figure 11 shows that about two-thirds of the potential drop occurs along the bus bar. Based on this observation, the bus bar is made thicker in the newest generation cells. This reduced the total  $R_{\text{g}}$  of the cells by a factor of two, quite a dramatic improvement for a device which had been thought to be almost completely optimised. For the first time the external resistive losses are reduced below the internal ones in our PERL cells. This constitutes a convincing success-story for simulation, as finding the right balance between shading and resistive losses would otherwise have required a tedious, expensive and time-consuming series of experiments.

This reduction contributed significantly to the latest world record for 1-sun silicon solar cell efficiency [1]. Figure 14 shows the improved voltage profile of cell zt11E, produced in the same batch as the record cells. The simulations show that for these later cells the grid is very close to optimal [20].

## 5 Conclusions

We have presented numerical simulations of a large,  $2 \times 2 \text{ cm}^2$  device with sub-micron feature sizes. Modelling the whole device was made possible by an innovative approach, which combines circuit simulation with 2D and 3D device simulations in a consistent model of a single, large device.

Figure 14: Comparison of measured MPP voltage profile between an older cell, w413-9, and a latest generation PERL cell, zt11E.

The simulations show excellent agreement with experimental data. They allowed us to determine accurately the series resistance, a major factor limiting solar cell performance, and resolve it into various contributions. This made it possible to clearly identify the dominant contribution to the series resistance and subsequently reduce that contribution by a modification of the contact geometry. The resulting reduction of series resistance contributed significantly to the most recent improvement in the efficiency world record for silicon solar cells.

## References

- [1] Jianhua Zhao, Aihua Wang, Pietro P. Altermatt, Stuart R. Wenham, and Martin A. Green, “24 % Efficient silicon solar cells”, in *1st World Conference on*

- Photovoltaic Energy Conversion*, Waikoloa, HI, USA, Dec. 1994, IEEE, pp. 1477–80.
- [2] Martin A. Green, K. Emery, Klaus Bücher, and David L. King, “Solar cell efficiency tables (Version 5)”, *Progress in Photovoltaics*, vol. 3, pp. 51–5, 1995.
- [3] Gernot Heiser, Armin G. Aberle, Stuart R. Wenham, and Martin A. Green, “Two-dimensional numerical simulations of high-efficiency silicon solar cells”, in *Proceedings of the 5th International Conference on Simulation of Semiconductor Devices and Processes*, Vienna, Austria, Sept. 1993, pp. 389–92, Springer Verlag.
- [4] J.L. Gray, R.J. Schwartz, and R.D. Nasby, “Two dimensional effects in conventional solar cells operated at high intensities”, in *International Electron Devices Meeting*. IEEE, 1982, pp. 107–10.
- [5] M. Ghannam, E. Demesmaeker, J. Nijs, R. Mertens, and R. van Overstraeten, “Two dimensional study of alternative back surface passivation methods for high-efficiency silicon solar cells”, in *Proceedings of the 11th European Photovoltaic Solar Energy Conference*, Montreux, Switzerland, Oct. 1992, pp. 45–8.
- [6] M. Schöfthaler, U. Rau, W. Füssel, and J.H. Werner, “Optimization of the back contact geometry for high efficiency solar cells”, in *Proceedings of the 23rd IEEE Photovoltaic Specialists Conference*, Louisville, KY, USA, 1993, IEEE, pp. 315–20.
- [7] Steffen Sterk and Stephan Glunz, “Simulation in high efficiency solar cell research”, in *Proceedings of the 5th International Conference on Simulation of Semiconductor Devices and Processes*, Vienna, Austria, 1993, pp. 393–6, Springer Verlag.
- [8] Steffen Sterk, J. Knobloch, and Wolfram Wettling, “Optimization of the rear contact pattern of high-efficiency silicon solar cells with and without local back surface field”, *Progress in Photovoltaics*, pp. 19–26, 1994.
- [9] Gernot Heiser and Armin G. Aberle, “Numerical modelling of non-ideal current-voltage characteristics of high-efficiency silicon solar cells”, in *5th International Workshop on Numerical Modeling of Processes and Devices for Integrated Circuits*, Honolulu, HI, USA, June 1994, IEEE, pp. 177–80.
- [10] Hiroyuki Ohtsuka, Yasuyuki Ohkura, Tsuyoshi Uematsu, and Terunori Warabisako, “Three-dimensional numerical analysis of contact geometry in back-contact solar cells”, *Progress in Photovoltaics*, pp. 275–85, 1994.
- [11] Martin A. Green, *Solar Cells*, Prentice-Hall, 1982.

- [12] Martin A. Green, *Silicon Solar Cells: Advanced Principles and Practice*, Bridge Printery, Sydney, Australia, 1995.
- [13] Armin G. Aberle, Pietro P. Altermatt, Gernot Heiser, Stephen J. Robinson, Aihua Wang, Jianhua Zhao, Ulrich Krumbein, and Martin A. Green, “Limiting loss mechanisms in 23-percent efficient silicon solar cells”, *Journal of Applied Physics*, vol. 77, pp. 3491–504, 1995.
- [14] Paul A. Basore, “Numerical modeling of textured silicon solar cells using PC-1D”, *IEEE Transactions on Electron Devices*, vol. 37, pp. 337–43, 1990.
- [15] Manuscript in preparation.
- [16] Armin G. Aberle, Gernot Heiser, and Martin A. Green, “Two-dimensional numerical optimisation study of the rear contact geometry of high-efficiency silicon solar cells”, *Journal of Applied Physics*, vol. 75, no. 10, pp. 5391–405, 1994.
- [17] Gernot Heiser, Pietro P. Altermatt, Aidan Williams, Alistair Sproul, and Martin A. Green, “Optimisation of rear contact geometry of high-efficiency silicon solar cells using three dimensional numerical modelling”, in *Proceedings of the 13th European Photovoltaic Solar Energy Conference*, Nice, France, Oct. 1995, To be published.
- [18] Stephen J. Robinson, Stuart R. Wenham, Pietro P. Altermatt, Armin G. Aberle, G. Heiser, and Martin A. Green, “Recombination rate saturation mechanisms at oxidised surfaces of high-efficiency silicon solar cells”, *Journal of Applied Physics*, vol. 78, pp. 4740–54, 1995.
- [19] Gernot Heiser, Pietro P. Altermatt, and James Litsios, “Combining 2D and 3D device simulation with circuit simulation for optimising high-efficiency silicon solar cells”, in *Proceedings of the 6th International Conference on Simulation of Semiconductor Devices and Processes*, Erlangen, Germany, Sept. 1995, pp. 348–51, Springer Verlag Vienna.
- [20] Pietro P. Altermatt, Gernot Heiser, Armin Aberle, Jianhua Zhao, Aihua Wang, Stephen J. Robinson, and Martin A. Green, “Spatially resolved analysis and minimisation of resistive losses in high-efficiency Si solar cells”, Subm. to *Journal of Applied Physics*, Dec. 1995.
- [21] ISE Integrated Systems Engineering AG, Zurich, Switzerland, *DESSIS 1.3.6: Manual*, 1994.